EPR and ENDOR Study of Radiation-Induced Radical Formation in Purines: Hypoxanthine Hydrochloride Monohydrate Crystals X-irradiated at 10 K

Sibel Tokdemir and William H. Nelson*

Department of Physics and Astronomy, Georgia State University, P.O. Box 4106, Atlanta, Georgia 30302-4106

Received: May 12, 2005; In Final Form: July 21, 2005

Electron paramagnetic resonance (EPR) and electron-nuclear double resonance (ENDOR) study of hypoxanthine·HCl·H$_2$O crystals irradiated at low temperatures (10 K) identified three radical species. In these crystals, the parent molecules exist in a cationic form with a proton at N7. R1 was the product of net hydrogen addition to N3 and exhibited α-proton hyperfine couplings to HC2, HN1, HC8, and HN3. The coupling to HC2 has an isotropic component smaller than usual, evidently an indication that the bonds to C2 are nonplanar. R2 was the product of net hydrogen loss from N7, equivalent to the one-electron oxidation product of neutral hypoxanthine, and exhibited α-proton hyperfine couplings to HC2 and HC8. Both couplings are characteristic of planar bonding arrangements at the centers of spin. R3 was provisionally identified as the product of net hydrogen addition to O6 and exhibited hyperfine α-proton couplings to HC8 and NH1. To identify the set of radicals, the experiments employed four crystal types: normal, deuterated only at NH positions, deuterated at HC8 and NH positions, and deuterated at HC8 only. The low-temperature data also showed clear evidence for H/D isotope effects in formation and/or stabilization of all radicals. To aid and support the identifications, the experimental results were compared to DFT calculations performed on a variety of radical structures plausible for the parent molecule and molecular packing within the crystal.
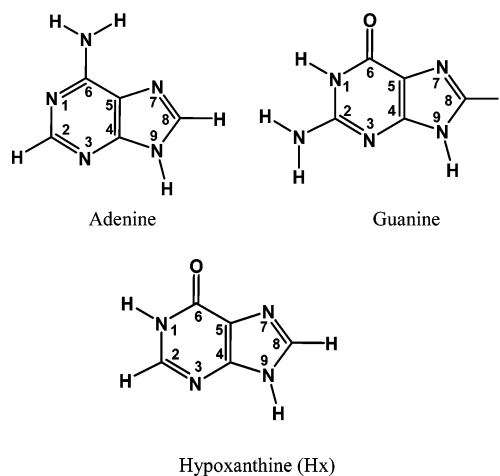
Introduction

Previous studies of adenine and guanine, the purine constituents of DNA, focused on the role of proton transfers in determining the radical structures resulting from exposure of the molecules to X-rays.[1] Immediately following ionization, the resulting holes and electrons are highly mobile and migrate throughout the system in a variety of processes such as tunneling and hopping.[2] Chemical products of the ionizations are the result of subsequent proton transfers that trap the electrons and holes as molecular reduction and oxidation products. Proton transfers automatically involve the surroundings of the ionized species. In molecular systems, therefore, hydrogen bonds and close molecular contacts, acting as either proton donors or proton acceptors, play a key role in determining whether the initial ion radicals are transient or lead to stable chemical products. Thus, the capability of a system to stabilize an ionization product can depend critically on the details of the molecular structure and how the product interacts with its surroundings.

For adenine, in either the neutral or the N1-protonated forms, the previous work found the major reduction product at low temperatures to be that of protonation at N3.[3] In contrast, the major reduction product of neutral guanine remains uncertain, whereas that of the guanine N7-protonated cationic form was identified as the result of protonation at O6. The major oxidation product of adenine and neutral guanine derivatives was deprotonation at the amino group. However, in some cases, N7 protonated guanine structures were found to deprotonate at the N7 position whereas the oxidation product was uncertain in others.[4]

Because the hydrogen bond donating and accepting abilities of the molecules, their environment, and their specific arrangements control the nature of the oxidation/reduction products actually detected in a molecular system, we have carried out a systematic investigation to identify radiation products stabilized in crystals. A major advantage of single crystals is that they provide well-defined molecular systems. To explore in more detail the ways in which intrinsic molecular properties and the nature of the molecular environment might combine to determine the radiation products stable enough for study, we sought systems similar to, yet different from, those studied previously.

Hypoxanthine, a purine derivative, was an attractive choice because of its structural similarities to both adenine and guanine. Specifically, like adenine but in contrast to guanine, hypoxanthine has an H rather than an amino at C2; however, like guanine but unlike adenine, hypoxanthine has an H at N1 and


Adenine　　　　　　　　Guanine

Hypoxanthine (Hx)

* Corresponding author. Ph: 404-651-1970. Fax: 404-651-1427. E-mail: wnelson@gsu.edu.

EPR/ENDOR of Radical Formation in Purines

J. Phys. Chem. A, Vol. 109, No. 39, 2005 **8733**

an oxygen at C6. Also, unlike both adenine and guanine, hypoxanthine has no exocyclic amino group. Thus, the structural differences among guanine, hypoxanthine, and adenine involve polar atoms, which are the major participants in hydrogen bonding.

As part of an earlier series of studies on net hydrogen addition to purine and pyrimidine constituents of DNA, Zehner et al. reported results from hypoxanthine hydrochloride monohydrate (hypoxanthine·HCl·H$_2$O, or Hx·HCl·H$_2$O) X irradiated at room temperature and at 77 K.[5] However, the earlier study provided little discussion on the nature and identity of the primary radicals stabilized at low temperatures. Therefore, we chose to undertake a detailed study of the Hx system, and this report describes the radicals identified from single crystals X irradiated and studied at liquid helium temperatures. (A previous report described radicals stable at room temperature in this system.[6]) Future work will focus on the radical formation mechanisms.

Methods

Good quality Hx·HCl·H$_2$O crystals suitable for EPR/ENDOR grew by slow evaporation at room temperature of solutions consisting of ca. 0.2 M hypoxanthine (Sigma H9377) in 1.5 N aqueous HCl. Growth under these low-pH conditions led to crystals in which the hypoxanthine molecule was present as a formal cation due to protonation at N7 as is indicated in the structure. Crystals with the easily exchangeable protons (those
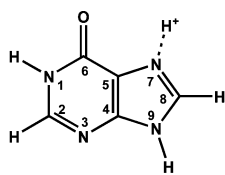
N7-protonated hypoxanthine

bonded to O and/or N) replaced by deuterons were grown in a corresponding manner from D$_2$O/DCl solutions except with the solutions in a closed desiccator.

Also, the proton at C8 is slowly exchangeable at elevated solution temperatures (ca. 100 °C).[7,8] This property makes it possible to prepare crystals with significant deuteration at C8 as well as at the easily exchangeable positions; material from this process also was used to prepare crystals deuterated mainly at C8 alone by subsequent growth from HCl/H$_2$O solutions. In summary, therefore, the results reported below come from crystals containing four different versions of the molecules: normal (N), D-exchange at the "easy" positions (E), D-exchange at C8 only (C8), and D-exchange at the "easy" positions and at C8 (F).

For the purposes of later discussion, we note that the proton at C2 also undergoes deuterium exchange at elevated solution temperatures but does so approximately 30 times more slowly than that at C8. Nevertheless, this means that the population of molecules includes those with deuterons only at C2 (D2H8), only at C8 (H2D8), at both (D2D8), and at neither (H2H8). With the rates given by Wong and Keck,[7] and the assumption that rates for exchange at either C2 or C8 are unaffected by previous exchange at the other position, the maximum concentration of the H2D8 species is approximately 85%. NMR assay of our "C8-deuterated" crystals (those actually used for the experiments) indicated that the total concentration of molecules with H's remaining at C8 was approximately 16% that of molecules with H's at C2. Under the assumption that the concentration of the D2H8 and D2D8 species are negligible

due to the much slower exchange at C2, the NMR data indicates our crystals contain the H2D8 species to a concentration slightly over 80%. We note, however, that the NMR data gave no direct indication of the actual concentration of D-containing molecules. In particular, the rate constants given by Wong and Keck indicate the peak concentration of the H2D8 species to occur after approximately 4−6 h incubation; for this reason we used 4 h in our preparation. These rates also indicate that incubation periods exceeding 100 hours yields the D2D8 species at concentrations of 90% or more. *Thus, aggressive efforts to maximize the exchange at C8 with extended incubation times also yield significant exchange at C2.*

Sletten and Jensen described a full crystallographic analysis of Hx·HCl·H$_2$O crystals and reported coordinates of all atoms, including the hydrogens.[9] They found the crystals to be monoclinic, to belong to space group $P2_1/c$, and to contain four molecules in the unit cell. In the unit cell, the molecules are arranged such that $\langle b \rangle$ lies in the molecular plane and makes approximately equal angles with the C2−H and C8−H bonds. As a result, it is not possible to distinguish these directions with the magnetic coupling parameters alone. Consequently, spectra from type C8 crystals (see above) provided key information for making the necessary distinctions.

Because of the monoclinic symmetry and the usual crystal habit, it was convenient to choose an orthogonal system based on the crystallographic $\langle a^* \rangle$, $\langle b \rangle$, and $\langle c \rangle$ directions for expressing the results. For these experiments, the crystals were irradiated at ca. 10 K, to doses typically in the range of 50−100 kGy with (0.4 mm) Al-filtered X-rays from a W-target tube operating at 55 kV. Following irradiation, and either without warming or under conditions of controlled warming, data were collected from the crystals for rotations about the $\langle a^* \rangle$, $\langle b \rangle$, and $\langle c^* \rangle$ axes using EPR, ENDOR, and EIE (ENDOR-induced EPR) methods. The data collection and data analysis methods were described previously.[10] (Because $\langle a^* \rangle$ and $\langle c^* \rangle$ are not orthogonal, the Schonland ambiguity [11] played a minor role in the results; the couplings listed in the tables are those giving the best statistical fits to the experimental data.) All spectra were obtained at K-band microwave frequencies (ca. 23.7 GHz) where the free-proton frequency for ENDOR was approximately 36.0 MHz.

Nitrogen hyperfine couplings reported in the tables were estimated from the EPR spectra with a spectrum-simulation approach using procedures based on the WINSIM program[12] as described previously.[6] In this case, however, the nitrogen coupling values listed were estimated from two to four simulations. To do so, it was assumed that the couplings are axially symmetric with the symmetry axis normal to the molecular plane of the molecule. With these assumptions, the expression for the coupling A_θ at any orientation making the angle θ to the symmetry axis is given by $A_\theta^2 = A_\parallel^2 \cos^2 \theta + A_\perp^2 \sin^2 \theta$. ($A_\parallel$ is the component parallel to the symmetry axis, and $A_\perp$ is the component normal to the symmetry axis or in the symmetry plane. In this case, the symmetry axis is the normal to the molecular plane, and was calculated for the a^*bc reference system from crystallographic data for each orientation.) The simulations gave values for A_θ at known values of θ; thus, with at least two A_θ values, it was possible to estimate $A_\parallel$ and $A_\perp$. The simulation methods also provided crude estimates for the relative concentrations of the radicals and their effective electronic g-values at the crystallographic orientations chosen for analysis.

For comparison to the experimental values, hyperfine couplings and electronic g-values were computed by use of Gaussian 03 (G03W).[13] All results were obtained using DFT
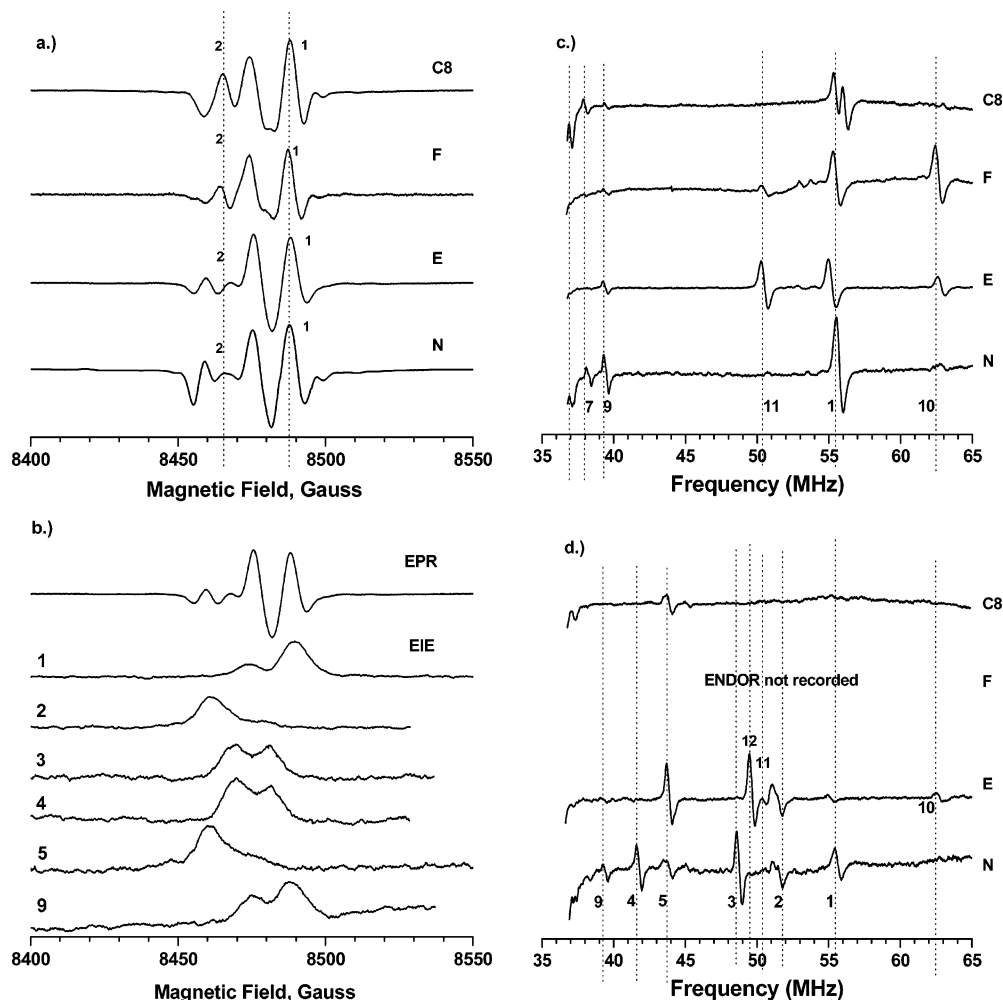
Figure 1. (a) EPR from the four Hx·HCl·H₂O crystal types described in the text. For each, the crystal's rotation axis was ⟨*b*⟩ and the magnetic field was in the molecular plane. (b) EIE patterns from the ENDOR lines indicated for type N crystals; the line numbers are those indicated in (c) and (d). (c) ENDOR from each crystal type at magnetic field position 1 as indicated in (a). The crystals were approximately at the same orientation, but there were slight differences. In particular, the rotation axis of the type C8 crystal was slightly misoriented, so the lines are doubled due to the magnetic site splitting. (d) ENDOR from field position 2 as indicated in (a). Note that no ENDOR was recorded at this position for Type F crystals.

methods with the B3LYP functional. To permit easier comparison of the computed coupling tensors to experiment, the initial structural coordinates were derived directly from the crystal data.[14] The standard procedure was to preoptimize the geometry with the 6-31G(d,p) basis set followed by a second optimization with 6-311G(2df,p) using the NOSYMM option in both steps; the couplings reported below are those from the 6-311G(2df,p) calculation. G03 reports electronic **g**-tensors in a nonsymmetrical form; however, these can be put into the standard symmetrical form by constructing $\mathbf{g}_e^2 = \mathbf{g}\mathbf{g}^T$. With this approach, the eigenvectors of $\mathbf{g}_e^2$ are also those of the standard $\mathbf{g}_e$ and the eigenvalues of $\mathbf{g}_e$ are the square roots of those from $\mathbf{g}_e^2$.[15]

Results and Discussion

Figure 1 shows EPR and ENDOR spectra from all crystal types following irradiation at 10 K (with no warming). For these spectra, the magnetic field was in the molecular plane for rotation of the crystal about ⟨*b*⟩, and the labels on the ENDOR indicate eleven of the twelve couplings detectable by ENDOR in this study. Figure 1b shows a series of EIE patterns from type *N* crystals for six of the interactions. These patterns can be grouped into three sets: set 1, from lines 1 and 9, generally located at high-field positions; set 2, from lines 2 and 5, generally located at low-field positions; and set 3, from lines 3

and 4, generally located between the other two sets. It is common that EIE patterns from overlapping EPR regions are not symmetrical, possibly due to effects on the ENDOR response of radical−radical cross relaxation,[16] and these patterns exhibit the asymmetrical behavior. Those associated with set 3 are more symmetrical, probably because the corresponding EPRs overlap on both the low-field and high-field sides. In summary, the EIE's indicate three distinct radical species trapped in the crystals.

EPR from all four crystal types shown in Figure 1a reveals relatively small but noticeable differences. Most noticeable is the smaller spectral extent from crystal types F and C8 in comparison with those of types E and N. Parts c and d of Figure 1 show ENDOR obtained from the high-field position for all crystal types and from an intermediate value for types N, E, and C8. For the high-field position (Figure 1c), these spectra reveal differences as listed below:

(i) Line 1 is present strongly in all types.

(ii) Line 7 is present in types N and C8, but not in types E and F.

(iii) Line 9 is strongly present in E and N, but weakly present in types F and C8.

(iv) Line 10 is barely noticeable in type N, strongly present in types E and F, but unnoticeable in type C8.

(v) Line 11 is strongly present in type E, clearly noticeable in type F, and absent in both types N and C8.

EPR/ENDOR of Radical Formation in Purines

J. Phys. Chem. A, Vol. 109, No. 39, 2005 **8735**

TABLE 1: Hyperfine Coupling Tensors for R1 Formed in Hx·HCl·H₂O X-Irradiated at 10 K

coupling	isotropic value[a]	principal value[a]	eigenvectors[b] $\langle a^* \rangle$	$\langle b \rangle$	$\langle c \rangle$
R1₁(HC2)	−15.22(7)	−42.05(5)	0.669(1)	∓0.291(1)	−0.684(2)
(line 1)		−14.11(5)	−0.744(2)	∓0.263(2)	−0.615(1)
		+10.52(11)	−0.001(0)	±0.920(2)	−0.392(2)
R1₂(HN3)	−7.77(4)	−16.11(2)	−0.327(4)	±0.920(2)	−0.216(1)
(line 7)		−11.80(5)	−0.730(2)	∓0.391(5)	−0.561(2)
		+4.61(6)	0.600(4)	±0.025(1)	−0.799(1)
R1₃(HN1)	−4.30(5)	−10.09(3)	−0.008(11)	±0.668(2)	−0.744(2)
(line 8)		−7.57(6)	−0.701(6)	∓0.534(9)	−0.473(2)
		+4.77(6)	0.713(5)	∓0.518(10)	−0.473(2)
R1₄(HC8)	−4.34(3)	−6.89(3)	0.552(4)	∓0.225(3)	−0.803(5)
(line 9)		−4.77(3)	−0.826(5)	∓0.020(5)	−0.563(1)
		−1.37(4)	0.110(3)	±0.974(5)	−0.197(6)
N1[c]	2.4	15.4	normal to the ring		
		−4.0	in the plane of the ring		
		−4.0	in the plane of the ring		
N3[c]	2.0	12.7	normal to the ring		
		−3.3	in the plane of the ring		
		−3.3	in the plane of the ring		
Directions from Crystal Structure					
base perpendicular[d]			−0.71988	−0.02021	−0.69380
C2−H bond direction			0.17746	0.95879	−0.22186
C8−H bond direction			0.17787	−0.96832	−0.17525
N3−H bond direction			0.67579	0.21401	−0.70534
N1−H bond direction			0.44554	−0.78338	−0.43337
N7−H bond direction			0.57404	0.54949	−0.60707
N9−H bond direction			0.69886	−0.08140	−0.71062

[a] Couplings in MHz. [b] Numbers in parentheses are the estimated standard deviations in the respective values as reported by the statistical analysis. Also, the signs of the $\langle b \rangle$ components reflect the indeterminacy imposed by the magnetic site symmetry of the $P2_1/c$ system. [c] Estimated from the simulation procedure. [d] Normal to least-squares plane through atoms N1 to N9.

For ENDOR from the intermediate-field EPR position (Figure 1d), the differences are

(i) line 2 is present in types N and E,

(ii) lines 3 and 4 appear only in type N,

(iii) line 5 is present in types N, E, and C8, and

(iv) line 12 is present in type E crystals, but absent in the others.

It was possible to collect data sufficient for calculating hyperfine coupling tensors for eleven of the twelve couplings; line 8 was within the free-proton region and not visible at the crystal orientation shown although it was possible to obtain a coupling tensor for it from data at other crystal orientations; likewise, line 6 was detectable at other orientations, but it was not possible to obtain enough data to extract a tensor.

Radical R1. ENDOR and EIE from the complete set of crystal orientations showed that lines 1, 7, 8, and 9 (Figure 1) were associated with each other; thus radical R1 evidently exhibits hyperfine interactions to four protons giving rise to these lines. Analysis of their angular dependence (see Supporting Information) led to the set of hyperfine couplings listed in Table 1. Couplings R1₁ (line 1) and R1₄ (line 9) are characteristic of CH α-proton hyperfine interactions because the eigenvectors ($\hat{V}_{mid}$) of the intermediate-magnitude hyperfine coupling components (a_{mid}) are approximately along the normal to the molecular plane (angular differences of 14° and 10°, respectively). In addition, the eigenvectors ($\hat{V}_{min}$) of the minimum-magnitude components (a_{min}) are approximately along the C2−HC2 or C8−HC8 bonds (angular differences of 14° and 4°, respectively).

Because of the unusual molecular symmetry relative to the crystallographic axes in Hx crystals, the eigenvectors alone are insufficient for assigning couplings R1₁ and R1₄ to HC2 or HC8; however, the presence of line 1 in all crystal types is clear
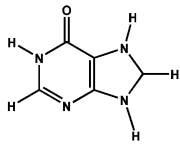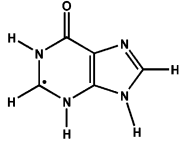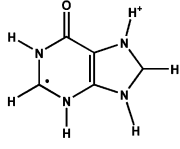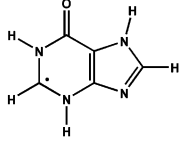
indication that it arises from HC2. Line 9 must therefore be the result of an HC8 interaction. We note that line 9 did not completely disappear in the C8-deuterated crystals; however, it was significantly reduced in strength, an overall behavior we attribute to the residual ca. 16% HC8 protons in types F and C8 crystals. Also we note that R1₁ has a somewhat unusual set of coupling values, a point to which we will return below.

Couplings R1₂ (line 7) and R1₃ (line 8) both arise from easily exchangeable protons, and the coupling values for each are characteristic of NH α-proton hyperfine interactions. $\hat{V}_{mid}$ from each are approximately normal to the molecular plane, although the angular differences are fairly large (22° and 32°, respectively). Because of the large angular differences, it is not possible to assign R1₃ from the coupling data alone—the bond directions closest to its $\hat{V}_{min}$ are N7−HN7 and N1−HN1 (angular differences of 11° and 22°, respectively). Likewise, the coupling data alone give no clear assignment for R1₂: its $\hat{V}_{min}$ is near the directions of the N9−HN9 bond as well as the bisector of C2−N3−C4 (angular differences of 8° and 13°).

The identity of R1 is suggested by coupling R1₁, evidently from HC2 and due to significant spin density at C2. However, the components of R1₁ are quite unusual in that the isotropic value (−15.2 MHz) is significantly less than is normal for the dipolar values (b_+ =25.7 MHz, b_0 = 1.11 MHz, and b_- = −26.8 MHz). In fact, estimation of $\rho(C2)$ from the isotropic component by the McConnell relation[17] using $Q^{\alpha}_{CH} = -70.0$ MHz[18] yields 0.22, whereas calculation from the b₊ dipolar component by the Gordy−Bernhard relation using $Q^z_{dip} = 38.7$ MHz[19] yields 0.66. This dramatic difference in estimated spin values is clear indication of bending at the site of unpaired spin and that the dipolar-based value ($\rho(C2) = 0.66$) is the more reliable.[20]

TABLE 2: Experimental Hyperfine Couplings (MHz) and Those Computed for Various Hx Structures Possibly Initiated by One-Electron Reduction

Structure	Atom	a_{iso}	b_-	b_0	b_+
Hx_{+7}^0	C2-H	-0.93	-0.82	-0.44	1.26
	C8-H	73.97	-24.18	-3.24	27.42
	N1-H	0.22	-0.84	-0.30	1.14
	N7-H	16.57	-12.52	-6.54	19.06
	N9-H	-0.47	-9.51	-4.88	14.40
	N1	-1.03	-0.85	0.34	0.52
	N3	0.62	-0.77	-0.51	1.28
	N7	4.75	-11.01	-10.61	21.62
	N9	1.41	-7.51	-7.06	14.57
Hx_{+3}^0	C2-H	24.68	-28.05	-2.28	30.32
	C8-H	-3.90	-2.63	-0.26	2.89
	N1-H	-10.86	-9.92	-4.98	14.91
	N3-H	8.32	-8.78	-6.28	15.06
	N9-H	-0.83	-1.41	-0.66	0.07
	N1	2.92	-8.45	-7.99	16.44
	N3	-0.26	-7.44	-7.04	14.49
	N7	-1.01	-1.53	0.71	0.82
	N9	0.38	-0.63	-0.43	1.06
$Hx_{+7,+3}^{+1}$ **(R1)**	C2-H	-10.6	-30.73	-0.65	31.38
	C8-H	-8.96	-5.22	0.05	5.18
	N1-H	-9.26	-7.73	-4.73	12.46
	N3-H	-5.11	-6.08	-4.74	10.82
	N7-H	1.17	-1.18	-0.47	1.65
	N9-H	-3.38	-2.07	-1.69	3.76
	N1	1.27	-6.62	-6.04	12.65
	N3	-1.09	-4.78	-4.18	8.96
	N7	-2.24	-2.44	1.18	1.26
	N9	1.28	-2.33	-2.15	4.48
$Hx_{+7,+3,-9}^0$	C2-H	22.87	-28.03	-2.32	30.35
	C8-H	-0.78	-0.81	-0.56	1.37
	N1-H	-9.41	-8.99	-4.83	13.82
	N3-H	-3.48	-11.05	-5.72	16.77
	N7-H	-0.26	-0.93	-0.74	1.67
	N1	2.27	-7.44	-6.97	14.40
	N3	1.83	-9.22	-8.82	18.04
	N7	-0.76	-0.19	0.02	0.16
	N9	0.46	-1.04	-0.69	1.73
Experiment	C2-H	-15.20	-26.83	1.11	25.72
	C8-H	-4.34	-2.54	-0.43	2.97
	N1-H	-4.30	-5.79	-3.27	9.07
	N3-H	-7.77	-8.34	-4.03	12.38
	N1	2.40	-6.40	-6.40	13.00
	N3	2.00	-5.35	-5.35	10.70

Such a large concentration of spin at C2 suggests R1's identity as the radical formed by net hydrogen addition to N3, similar to a structure known from previous study of adenine derivatives.[21] To aid in the identification of R1, and in assigning the remaining couplings, we calculated couplings expected for several one-electron reduction products, those from electron addition alone, from net hydrogen addition to N3 with the proton at N7 remaining, and from tautomeric rearrangements of the parent structure leading to a proton attached to N3; the results are listed in Table 2.

Inspection of Table 2 shows that three of the structures (Hx_{+3}^0, $Hx_{+7,+3}^{+1}$, and $Hx_{+7,+3,-9}^0$) exhibit large couplings to HC2 comparable to that observed. It is now recognized that dipolar coupling values are more reliable than isotropic values for comparison to experiment. From that perspective, the structures with and without a proton at N7 give virtually indistinguishable sets of hyperfine couplings. Based on the computations, it is possible to assign line 7 to HN3 and line 8 to HN1. Although the calculated sets of couplings from the three structures compare reasonably well with the experimental data, no set was markedly better than the others. Primarily because its formation requires fewer steps—electron addition followed

by proton addition at N3, we favor the $Hx_{+7,+3}^{+1}$ version as the structure for R1. (In connection with the isotope effects

$Hx_{+7,+3}^{+1}$ *(R1)*
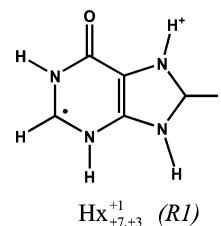
described below, it should be noted that we cannot rule out coexistence of combinations of the N3-protonated structures.)

In addition to the coupling values, eigenvectors of the dipolar couplings give geometry information on the radical's structure. Computed eigenvectors for the HC2 coupling of the $Hx_{+7,+3}^{+1}$ structure were different from the experimental eigenvectors by 0.6°, 31.8°, and 31.9°, respectively, for $\hat{V}_{max}$, $\hat{V}_{mid}$, and $\hat{V}_{min}$. This set of values indicates that the respective $\hat{V}_{mid}$ and $\hat{V}_{min}$ directions are related by a rotation about $\hat{V}_{max}$. Moreover, because the initial structure for the computations was virtually

EPR/ENDOR of Radical Formation in Purines

J. Phys. Chem. A, Vol. 109, No. 39, 2005 **8737**

TABLE 3: Comparison of Experimental Eigenvectors to Those Computed for the $Hx^{+1}_{+7,+3}$ Structure Attributed to R1

	as calculated			transformed			measured			
	$\langle a^* \rangle$	$\langle b \rangle$	$\langle c \rangle$	$\langle a^* \rangle$	$\langle b \rangle$	$\langle c \rangle$	$\langle a^* \rangle$	$\langle b \rangle$	$\langle c \rangle$	$\delta\phi$ (deg)
					HC2					
$\hat{V}_{max}$	0.6788	−0.2953	−0.6723	0.6554	−0.2960	−0.6948	0.669	−0.291	−0.684	0.94
$\hat{V}_{mid}$	0.6207	−0.2585	0.7402	−0.7545	−0.2971	−0.5852	−0.744	−0.263	−0.615	2.02
$\hat{V}_{min}$	0.3924	0.9198	−0.0077	−0.0334	0.9078	−0.4181	−0.001	0.920	−0.392	2.39
					HC8					
$\hat{V}_{max}$	−0.6725	−0.2141	0.7085	−0.6770	−0.2142	0.7042	−0.552	−0.225	0.803	9.12
$\hat{V}_{mid}$	0.7184	0.0415	0.6944	−0.7210	0.0011	−0.6929	−0.826	0.020	−0.563	9.70
$\hat{V}_{min}$	0.1781	−0.9759	−0.1259	0.1477	−0.9768	−0.1552	0.110	−0.974	−0.197	3.45
					HN1					
$\hat{V}_{max}$	0.6301	0.7432	−0.2249	0.1801	0.7306	−0.6586	−0.008	0.668	−0.744	12.42
$\hat{V}_{mid}$	0.6295	−0.3193	0.7083	−0.7212	−0.3572	−0.5935	−0.701	−0.534	−0.473	12.31
$\hat{V}_{min}$	−0.4546	0.5879	0.6691	−0.6689	0.5819	0.4626	−0.713	0.518	0.473	4.34
					HN3					
$\hat{V}_{max}$	0.2959	0.8997	0.3210	0.3576	0.8814	−0.3088	−0.327	0.920	−0.216	6.01
$\hat{V}_{mid}$	0.5284	−0.4341	0.7297	−0.7355	−0.4696	−0.4885	−0.730	−0.391	−0.561	5.97
$\hat{V}_{min}$	0.7958	−0.0463	−0.6038	0.5755	−0.0525	−0.8161	0.600	0.025	−0.799	5.08

planar with $\hat{V}_{max}$ lying in the plane, this relationship could indicate that the actual and computed structures are related by a reflection into the molecular symmetry plane. In essence, this means that the actual and computed structures might be equally deformed, but on opposite sides of the symmetry plane. To test this possibility, we transformed the computed vectors by reflection into the least-squares plane through the ring atoms (N1 through N9 of the initial crystal-structure-based coordinates). Table 3 shows the vectors directly from the computation, those after transformation, the experimental vectors, and the angular differences between the experimental and transformed vectors. The correspondence between the computed and experimental values is remarkably close.

After this, we recomputed the radical's geometry with the starting coordinates reflected through the symmetry plan; the optimized geometry from that computation was virtually identical to that obtained by the reflection operation on the initial optimized structure. As well, the energies of the two structures were virtually identical; thus they are equally valid optimized structures. A final point is that we also compared the sets of eigenvectors for the other N3-addition structures and found all to correspond reasonably well with experiment (Supporting Information, Table S1), but the $Hx^{+1}_{+7,+3}$ structure was best.

As was mentioned above, the isotropic component of the HC2 α-coupling is substantially smaller than usual in relation to the dipolar component. This is a known result of tetrahedral character in the bonds at the center of spin, which was described in detail earlier.[20] At the C2 position of Hx, this can occur by movement of the N1−C2−N3 set of bonds out of the molecular plane, by bending of the C2−HC2 bond out of the plane, or by any combination of these, which leads to the net result of pyramidal character at the site of spin. Figure 2 shows the optimized geometry calculated for the $Hx^{+1}_{+7,+3}$ structure that exhibits this geometry. For example, calculation on the $Hx^{+1}_{+7,+3}$ structure gave the isotropic value −10.59 MHz with $\hat{V}_{mid}$ approximately 20° from the normal to the ring; experiment gave the isotropic value −15.22 MHz with $\hat{V}_{mid}$ approximately 17° from the normal. For a completely planar arrangement of N1, C2, N3, and HC2 the isotropic value would be approximately −50 MHz according to calculations and $\hat{V}_{mid}$ would be along the normal to the ring. Thus, the angular difference between the experimental result and the normal to the ring indicates significant bending at C2, and it is consistent with the calculations because the more negative (larger magnitude)

experimental value indicates less bending than predicted by the calculations.
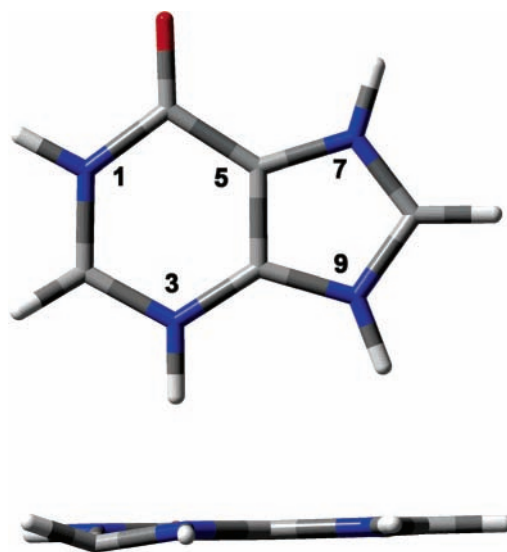
Figure 2. Geometry-optimized $Hx^{+1}_{+7,+3}$ structure attributed to R1. The lower view, approximately along the N3−HN3 bond, shows the bending at C2 predicted by the computation.

It is also useful to note that the set of coupling values in the table for the electron adduct Hx^0_{+7} compares well with the others if the identities of the atoms are ignored; i.e., HC8 couplings are comparable to those of HC2, HN7 and HN9 couplings are comparable to those of HN1 and HN3, and N7 and N9 couplings are comparable to those of N1 and N3. Thus, because the crystal geometry made the C2−H and C8−H directions indistinguishable insofar as the magnetic resonance data is concerned, the deuterium exchange information was critical to identifying this radical species. This is an important point because the earlier study also used crystals of C8-deuterated material. In the lower right panel of their Figure 5, they show evidence that C8-deuteration caused the high-field EPR doublet (corresponding to our line 1) to collapse to a singlet.[5] This is in contrast to our results where no such collapse occurred. Because our crystals were assayed by NMR methods, there is no doubt that line 1 described here is the result of HC2. One explanation for the earlier result is that the authors used long incubation times for the HC8 deuterium exchange process

TABLE 4: Hyperfine Coupling Tensors for ENDOR Lines 10 and 11 Formed in Hx·HCl·H₂O X-Irradiated at 10 K

coupling	isotropic value[a]	principal value[a]	eigenvectors[b]		
			⟨a*⟩	⟨b⟩	⟨c⟩
RI$_4$(HC2)[c]	−27.9(2)	−55.9(1)	0.630(1)	∓0.309(3)	−0.713(4)
(line 10)		−26.8(1)	0.697(5)	∓0.180(5)	0.694(1)
		−1.0(4)	0.343(2)	±0.934(2)	−0.102(6)
RI$_5$(HC8?)[c]	−19.7(0)	−32.0(0)	0.7359(3)	±0.2504(6)	−0.6291(12)
(line 11)		−18.2(0)	0.6485(8)	±0.0062(16)	0.7612(2)
		−9.0(0)	0.1945(5)	∓0.9681(10)	−0.1578(15)
		Directions from Crystal Structure			
base perpendicular[d]			−0.71988	−0.02021	−0.69380
C2−H bond direction			0.1775	0.9588	−0.2219
C8−H bond direction			0.1779	−0.9683	−0.1753

[a] Couplings in MHz. [b] Numbers in parentheses are the estimated standard deviations in the respective values as reported by the statistical analysis. Also, the signs of the ⟨b⟩ components reflect the indeterminacy imposed by the magnetic site symmetry of the $P2_1/c$ system. [c] Lines associated with radical R1 indicating H/D isotope effects as discussed in the text. [d] Normal to least-squares plane through atoms N1 to N9.
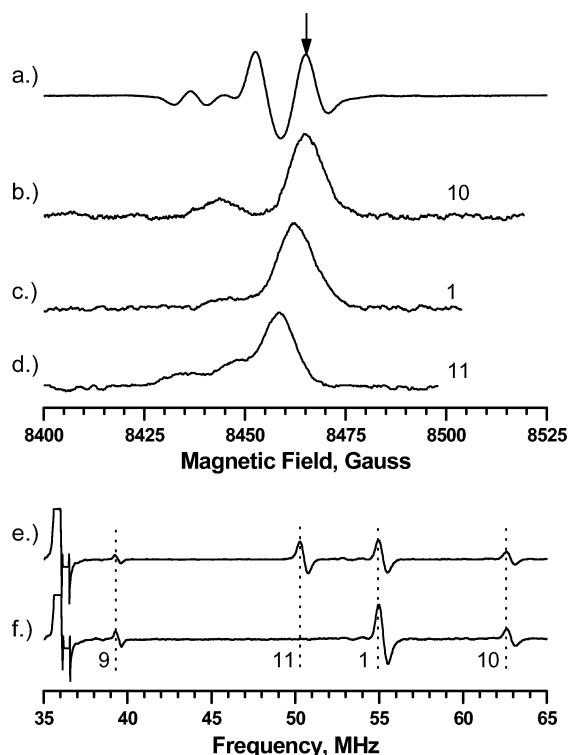
Figure 3. ENDOR and EIE patterns from type E crystals for rotation about ⟨b⟩ with the magnetic field in the molecular plane: (a) EPR at 10 K with the arrow indicating the field setting used for ENDOR patterns e and f; (b) EIE from line 10 at 10 K; (c) EIE from line 1; (d) EIE from line 11; (e) ENDOR at 10 K before warming; (f) ENDOR at 10 K following warming to 40 K. Note the absence of line 11.

and thereby also obtained significant exchange of HC2 (see Methods). By spectrum simulation methods, we estimate that exchange of HC2 greater than 90% is necessary to obtain an EPR pattern with an unnoticeable residue of the high-field doublet as is shown in their figure.

Isotope Effects in Formation of R1. Lines 10 and 11 exhibit evidence for isotope effects in formation of the radicals from which they arise. Specifically, Figure 1c shows that the ENDOR response for line 10 in type N crystals is barely noticeable but is much stronger in crystal types E and F. Likewise, line 11 is strong in type E crystals, easily noticeable in those of type F, and unnoticeable in types N and C8. Figure 3b−d shows EIE patterns from lines 10 and 11 in comparison with that of line 1. Although the patterns peak at slightly different field values, indicating a combination of different hyperfine couplings and different *g*-shifts, they are similar enough to suggest a relation-

ship. On warming the crystal to 40 K and recooling to 10 K, line 11 was absent and ENDOR from line 1 seemed stronger (Figure 3e,f). In contrast, line 10 persisted on warming to 140 K although weakened considerably. It seems unlikely that deuterium exchange would lead to the formation of totally new products; rather, it is more likely that these behaviors reflect the incomplete formation of products found in the type N crystals. Specifically, a reasonable speculation is that lines 10 and 11 both arise from radical structures associated with proton transfers in type N crystals; however, at the low experimental temperatures, H/D kinetic isotope effects[23] may lead the more massive deuterons (vs protons) to transfer incompletely, if at all.

Table 4 lists the hyperfine parameters for lines 10 and 11 as extracted from their angular dependence (see Supporting Information). Line 10 evidently is from HC2 because it appears strongly in the crystals deuterated at C8. In addition, the dipolar component of its coupling is very similar to that of line 1; however, its isotropic coupling is larger, although still not like that expected from a planar bonding structure at the C2 position. The similarity of hyperfine couplings for lines 1 and 10 in combination with their similar EIE patterns, make it reasonable to associate line 10 with a conformer of R1 in which the radical structure is less bent at C2. Because R1 is the result of a proton transfer to N3 (evidently from water), we further speculate that the bending at C2 is associated with other easily exchangeable positions in the molecule, probably via vibrational modes, such that the additional mass at those sites inhibits the bending at C2. We note that there was no evidence for growth in either line 1 or line 10 at the expense of the other on warming the crystals to 140 K where both were virtually reduced to noise level in the ENDOR.

Line 11 was strong in type E crystals, but less so in those of type F. This clearly indicates a role of deuteration at C8, along with that of the easily exchangeable positions, in formation of the product giving this line. Because line 11 did not appear in type C8 crystals, it is clear that deuteration at C8 is an inhibiting factor. One possibility is that line 11 is from HC8 and the reduction in its ENDOR response in type F crystals, vs that in type E, reflects the residual ca. 16% HC8's remaining in types F and C8 crystals. (Otherwise, based on the eigenvectors, line 11 must be from HC2.) In combination with the apparent increase in the ENDOR response of line 1 when line 11 disappears near 40 K, this suggests that line 11 is due to incomplete proton transfer in the formation of product R1. If so, line 11 should reflect properties of the primary electron-addition product, Hx_{+7}^0; however, the coupling parameters

EPR/ENDOR of Radical Formation in Purines

J. Phys. Chem. A, Vol. 109, No. 39, 2005 **8739**

TABLE 5: Hyperfine Couplings for R2[a] Formed in Hx·HCl·H₂O X-Irradiated at 10 K

coupling	isotropic value[a]	principal value[a]	eigenvectors[b]		
			$\langle a*\rangle$	$\langle b\rangle$	$\langle c\rangle$
R2₁(HC8)	−21.9(0)	−31.9(0)	0.623(1)	±0.325(1)	−0.712(2)
(line 2)		−23.8(0)	−0.761(1)	∓0.042(1)	−0.647(0)
		−10.1(0)	0.181(1)	∓0.945(1)	−0.273(1)
R2₂(HC2)	−10.9(0)	−15.9(0)	−0.799(1)	±0.035(2)	0.600(2)
(line 5)		−13.6(0)	−0.598(2)	∓0.140(2)	−0.789(0)
		−3.2(0)	−0.057(2)	±0.990(1)	−0.133(2)
R2₃(HC8)[c]	−20.0(0)	−30.7(0)	0.726(1)	±0.324(1)	−0.607(2)
(line 12)		−21.4(0)	−0.646(1)	±0.019(2)	−0.763(0)
		−7.9(0)	0.236(1)	∓0.946(1)	−0.224(2)
N1[d]	1.20	6.07	normal to the ring		
		−1.24	in the plane of the ring		
		−1.24	in the plane of the ring		
N3[d]	1.85	10.50	normal to the ring		
		−2.49	in the plane of the ring		
		−2.49	in the plane of the ring		
Directions from Crystal Structure					
base perpendicular[e]		−0.71988	−0.02021	−0.69380	
C2−H bond direction			0.17746	0.95879	−0.22186
C8−H bond direction			0.17787	−0.96832	−0.17525

[a] Couplings in MHz. [b] Numbers in parentheses are the estimated standard deviations in the respective values as reported by the statistical analysis. Also, the signs of the $\langle b\rangle$ components reflect the indeterminacy imposed by the magnetic site symmetry of the $P2_1/c$ system. [c] Observed only in type E crystals. See the text for a discussion of this coupling. [d] Estimated from the simulation procedure. [e] Normal to least-squares plane through atoms N1 to N9.

extracted for line 11 (Table 4) are unlike those calculated for HC8 of the Hx$^0_{+7}$ structure as listed in Table 2. In fact, the hyperfine coupling indicated by line 11 is more like those of lines 2 and 12 to be discussed below. However, EIE patterns from all indicate the product associated with line 11 gives a *g*-shift significantly different from those associated with lines 2 and 12. Thus, despite the evident connection with R1 and deuteration, the nature of the product yielding line 11 remains an open question.

Radical R2. EIE patterns (Figure 1b) indicated that lines 2 and 5 were associated with each other and therefore that radical R2 exhibits hyperfine interactions to (at least) two protons. Analysis of the angular dependence of lines 2 and 5 (Supporting Information) led to the set of hyperfine couplings listed in Table 5. Couplings R2₁ (line 2) and R2₂ (line 5) are characteristic of CH α-proton interactions with $\hat{V}_{mid}$ for both approximately along the normal to the molecular plane (angular differences of 4° and 11°, respectively). Also, these couplings could be from either HC2 or HC8 because their $\hat{V}_{min}$ directions are approximately along the respective bonds. Because line 2 is absent and line 5 is present in type C8 crystals, we assigned coupling R2₁ (line 2) to HC8 and R2₂ (line 5) to HC2. For line 2, spin estimates from the McConnell and the Gordy−Bernhard methods are identical (0.31), whereas those from line 5 are virtually identical (0.16 vs 0.20). Thus, there is no evidence for bending at C8, and insignificant evidence for bending at C2.

To aid in identifying the radical giving lines 2 and 5, we calculated couplings expected for several one-electron oxidation products of the parent molecule; the results are listed in Table 6. From inspection of the table, it is clear that the best match is the set of values from the structure Hx^{+1}. Table 7 shows the correspondence between the experimental eigenvectors and those computed for the Hx^{+1} structure; the correspondence of these also is very good. This structure is equivalent to the one-electron-oxidation product of the neutral hypoxanthine molecule; evidently, in this case, it was formed by electron-loss followed by deprotonation at N7. A final point is that warming studies also showed that the EPR from R2 persisted on warming the
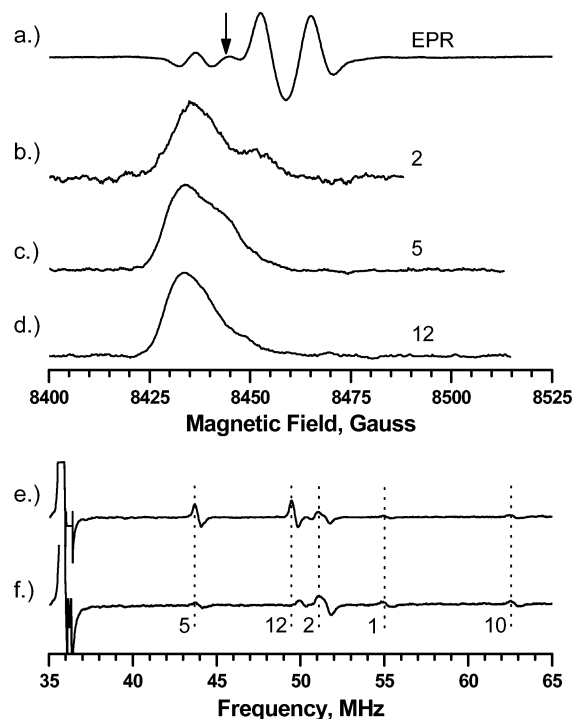
Figure 4. ENDOR and EIE patterns from type E crystals for rotation about $\langle b\rangle$ with the magnetic field in the molecular plane: (a) EPR at 10 K with the arrow indicating the field setting used for ENDOR patterns e and f; (b) EIE from line 2 at 10 K; (c) EIE from line 5; (d) EIE from line 12; (e) ENDOR at 10 K before warming; (f) ENDOR at 10 K following warming to 60 K. Note the absence of line 12.

type N crystals to 160 K. (See Figure S1 in the Supporting Information.) In the previous report describing the room-temperature results, it was proposed that net OH addition to C8 was the product of "attack" on a favorably positioned water by Hx^{+1}, i.e., R2,[6,20] and the warming data supports the feasibility of that proposal.

Isotope Effects in Formation of R2. Figure 1d shows that line 12 appeared in type E crystals but was absent in both types

TABLE 6: Hyperfine Coupling Constants (MHz) Computed for Various Hx Structures Derived from One-Electron Oxidation Events

Structure	Atom	a_{iso}	b_-	b_0	b_+
Hx^{+1} **(R2)**	C2-H	-7.84	-5.38	-1.91	7.29
	C8-H	-21.76	-12.32	-1.53	13.84
	N1-H	-4.43	-2.72	-1.97	4.68
	N9-H	1.45	-2.28	0.99	1.29
	N1	0.50	-2.28	-2.06	4.34
	N3	2.80	-5.35	-5.09	10.44
	N7	-1.31	-0.80	-0.56	1.35
	N9	-4.70	-3.30	1.49	1.81
Hx^{+2}_{+7}	C2-H	-2.02	-2.89	-2.64	5.54
	C8-H	-9.69	-5.78	1.34	7.13
	N1-H	-8.35	-4.01	-3.33	7.34
	N7-H	-2.14	-2.77	-0.72	3.49
	N9-H	-0.35	-1.89	-0.16	2.05
	N1	2.94	-4.53	-4.26	8.79
	N3	8.23	-12.08	-11.84	23.93
	N7	-2.52	-1.13	-0.89	2.01
	N9	-1.69	-0.94	0.31	0.63
$Hx^{+1}_{7,-1}$	C2-H	6.97	-3.29	-1.35	4.64
	C8-H	-4.91	-3.26	-0.90	4.16
	N7-H	-0.31	-2.30	0.04	2.26
	N9-H	-2.06	-1.77	-0.97	2.74
	N1	6.26	-10.04	-9.83	19.87
	N3	11.67	-16.53	-16.29	32.82
	N7	-2.60	-0.09	-0.03	0.12
	N9	0.46	-0.97	-0.72	1.69
$Hx^{+1}_{+7,-9}$	C2-H	-8.87	-6.10	-1.95	8.05
	C8-H	-8.90	-5.75	-1.58	7.34
	N1-H	-3.48	-2.77	-0.83	3.61
	N7-H	-7.25	-4.99	-3.28	8.27
	N1	-0.52	-1.37	-1.19	2.55
	N3	2.39	-5.08	-4.84	9.92
	N7	0.59	-4.61	-4.29	8.90
	N9	-1.34	-2.46	1.13	1.34
Experiment	C2-H	-10.9	-5.0	-2.7	7.7
	C8-H	-21.9	-10.0	-1.9	11.8
	N1	1.20	-2.44	-2.44	4.87
	N3	1.85	-4.34	-4.34	8.65

TABLE 7: Comparison of the Experimental and Computed Eigenvectors for the Hx^{+1} Structure Attributed to R2

	experiment			computation			
	$\langle a^* \rangle$	$\langle b \rangle$	$\langle c \rangle$	$\langle a^* \rangle$	$\langle b \rangle$	$\langle c \rangle$	$\delta\phi$ (deg)
			HC2				
$\hat{V}_{max}$	0.6230	0.3250	-0.7120	-0.6571	-0.3213	0.6819	2.19
$\hat{V}_{mid}$	-0.7610	-0.0420	-0.6470	0.7155	0.0190	0.6984	4.28
$\hat{V}_{min}$	0.1807	-0.9448	-0.2733	-0.2373	0.9468	0.2174	4.56
			HC8				
$\hat{V}_{max}$	-0.7990	0.0350	0.6000	-0.6960	0.1063	0.7101	9.64
$\hat{V}_{mid}$	-0.5980	-0.1400	-0.7890	0.7154	0.0186	0.6985	11.01
$\hat{V}_{min}$	-0.0570	0.9900	-0.1330	0.0610	0.9942	-0.0889	6.97

N and C8. Table 5 shows the coupling tensor extracted from the angular dependence (Supporting Information); line 12 is from HC8 because it is unnoticeable in type C8 crystals. Figure 5 shows EIE patterns from line 12 in comparison to those of lines 2 and 5. The similarity between the couplings indicated by lines 2 and 12, and the similar g-shifts exhibited by the EIE patterns, suggest a connection between R2 and the radical responsible for line 12. As was discussed for R1, it seems most reasonable that these effects indicate a role of deuteration in the mechanisms by which R2 formed. This is further suggested by the behavior of lines 2, 5, and 12 on warming the type E crystals as shown in Figure 4e,f. In them, line 5 appears to decrease in intensity as line 12 disappears at 60 K. Consequently, one possibility is that R2 appears in two conformers, dependent on the deuteration state, in which the coupling associated with line 5 is the same in both, but the coupling associated with lines 2 and 12 is slightly different in the two.

Radical R3. EIE patterns shown in Figure 1b indicated that lines 3 and 4 arose from the same radical. Analysis of their angular dependence (Supporting Information) led to the couplings listed in Table 8. The coupling associated with line 3 is fairly normal for a CH α coupling: the isotropic component indicates spin of 0.26, and the dipolar component indicates spin of 0.24. Its eigenvectors indicate either HC2 or HC8 as the coupling proton. With the near-zero minimum component, line 4 indicates a coupling like that frequently seen for NH protons. Its eigenvectors correspond most closely to those associated with HN1.

Most remarkable about lines 3 and 4 is that they were detected only in type N crystals, a property that also indicates a significant isotope effect in their formation. The absence of lines 3 and 4 in all other crystal types hinders definite assignments of the couplings to specific protons. On the basis of the likelihood that R3 forms by a proton-transfer inhibited by the presence of

EPR/ENDOR of Radical Formation in Purines

J. Phys. Chem. A, Vol. 109, No. 39, 2005 **8741**

TABLE 8: Hyperfine Couplings for R3 Formed in Hx·HCl·H$_2$O X-Irradiated at 10 K

coupling	isotropic value[a]	principal value[a]	eigenvectors[b]		
			$\langle a^*\rangle$	$\langle b\rangle$	$\langle c\rangle$
R3$_1$(HC8)	−18.1(0)	−25.4(0)	0.616(2)	±0.347(2)	−0.707(3)
(line 3)		−20.0(0)	0.763(2)	∓0.038(2)	0.646(1)
		−8.8(0)	0.197(2)	∓0.937(3)	−0.288(3)
R3$_2$(HN1)	−12.2(0)	−21.3(1)	0.365(4)	∓0.719(2)	−0.591(2)
(line 4)		−14.0(0)	0.858(1)	∓0.013(2)	0.514(1)
		−1.3(1)	0.362(2)	∓0.695(4)	−0.622(2)
N1[c]	9.94	12.21	normal to the ring		
		−6.10	in the plane of the ring		
		−6.10	in the plane of the ring		
N3[c]	3.95	6.47	normal to the ring		
		−3.25	in the plane of the ring		
		−3.25	in the plane of the ring		
N7[d]	3.56	10.58	normal to the ring		
		−5.29	in the plane of the ring		
		−5.29	in the plane of the ring		
Directions from Crystal Structure					
base perpendicular[d]			0.71988	0.02021	0.69380
C8−H bond direction			0.17787	−0.96832	−0.17525
N1−H bond direction			0.44554	−0.78338	−0.43337

[a] Couplings in MHz. [b] Numbers in parentheses are the estimated standard deviations in the respective values as reported by the statistical analysis. Also, the signs of the $\langle b\rangle$ components reflect the indeterminacy imposed by the magnetic site symmetry of the $P2_1/c$ system. [c] Estimated from the simulation procedure. [d] Normal to least-squares plane through atoms N1 to N9.

deuterons in all crystal forms other than N, we computed the couplings expected for several tautomeric structures related to the protonation of the one-electron reduction product at the position O6. This choice was guided by previous work with guanine whose molecular structure is similar.[10]

Hyperfine coupling values from the computations are shown in Table 9 along with the experimental values for reference. Of these, the HC8 values from Hx$^0_{+6,+7,−9}$ best match those from the experiment and the computed values for HN1 are reasonable matches. Computed couplings for the more straightforward Hx$^{+1}_{+7,+6}$ structure also match experiment reasonably well except for those of HC8, the computed values for which are two times too large. (Computed values for both structures predict large couplings to the HO6 proton. However, this is a $^\bullet$COH$_\beta$ coupling from which the isotropic value depends on the extent to which the H$_\beta$ proton is out of the molecular plane. In a crystal, it is common that hydrogen bonding constrains the H$_\beta$ to lie in the plane.) Table 10 shows the correspondence between the experimental eigenvectors and those of the two structures with the most favorable matches to the computed couplings; neither case is decisively better.
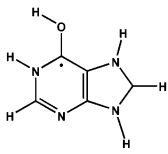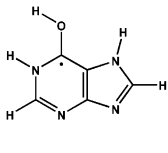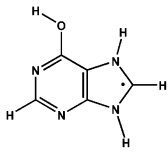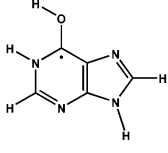
Thus, because of its better correspondence to the experimental HC8 coupling, we conclude that the Hx$^{+1}_{+7,+6,−9}$ structure fits the data better than the others listed in Table 10. This structure is reasonable because its formation requires gain of a proton at O6 and loss of a proton at N9 for the net result of no change in protonation. This is feasible in the crystal because the molecules are packed in layers with O6 of one molecule serving as the hydrogen bond acceptor for HN9 of a coplanar neighboring molecule. Thus, it is conceivable that the addition of HO6 can be the result of one-electron reduction followed by transfer of HN9 from a neighboring molecule; concurrently, HN9 of the O6-protonated product can transfer to O6 of a neighbor. This mechanism also is consistent with the H/D kinetic isotope effect[23] because the energy necessary for the transfers might be marginally available at the low experimental temperatures. In such a case, the additional mass of a deuteron could inhibit formation of the species in all crystals other than type N.
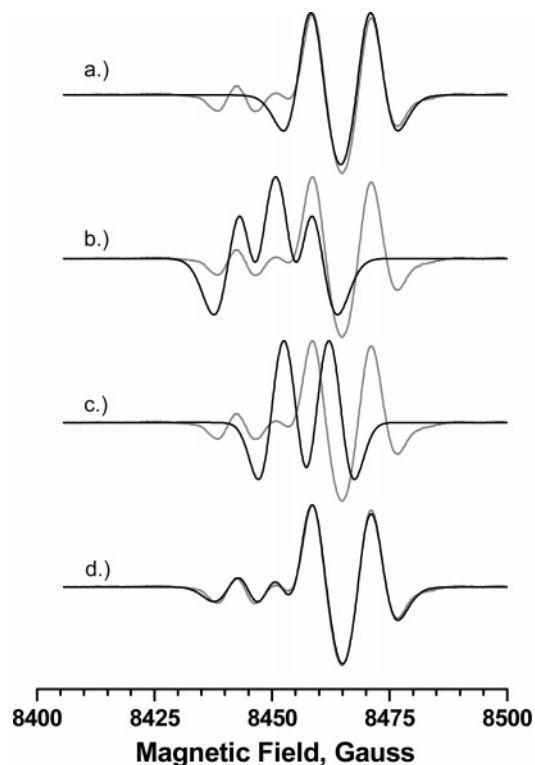
Figure 5. Reconstruction of the experimental (second derivative) EPR pattern from type N crystals using the optimized patterns derived by the WINSIM procedure. The experimental pattern is that obtained with the magnetic field in the molecular plane for rotation about $\langle b\rangle$. (a) Experimental (shaded) vs simulation for R1 only. (b) Experimental (shaded) vs simulation for R2 only. (c) Experimental vs simulation for R3 only. (d) Experimental (shaded) vs simulation composite. For the composite, the contributions from R1−R3 are not the amounts shown in (a)−(c); those amplitudes were increased for visibility purposes.

Spectrum Simulations. Figure 5 shows results from the spectrum simulation procedure based on WINSIM for the case where the magnetic field was in the molecular plan for rotation about $\langle b\rangle$. For the optimized composite spectrum shown in

TABLE 9: Experimental Hyperfine Couplings (MHz) and Those Computed for the O6-Hydrogenated Hx Radicals Indicated

Structure	Atom	a_{iso}	b_-	b_0	b_+
$Hx^{+1}_{+7,+6}$	C2-H	0.65	-2.31	0.25	2.07
	C8-H	-32.09	17.84	1.23	16.61
	O6-H	59.34	-5.16	-4.12	9.28
	N1-H	-9.81	-8.51	-2.98	11.49
	N7-H	-6.39	-3.68	-3.34	7.02
	N9-H	2.89	-2.39	-0.27	2.66
	N1	3.68	-6.83	-6.67	13.50
	N3	3.37	-5.01	-4.87	9.88
	N7	1.14	-4.07	-3.83	7.90
	N9	-6.80	-4.35	2.09	2.26
$Hx^0_{+6,+7,-9}$ *(R3)*	C2-H	0.018	-2.67	-0.09	2.76
	C8-H	-17.17	-9.97	0.36	9.61
	O6-H	38.68	-9.63	-6.25	15.88
	N1-H	-7.32	-9.84	-4.72	14.56
	N7-H	-0.40	-2.68	0.30	2.38
	N1	5.08	-8.02	-7.81	15.84
	N3	2.50	-4.49	-4.49	8.79
	N7	-0.37	-0.58	-0.21	0.79
	N9	-3.74	-4.87	2.34	2.54
$Hx^0_{+6,+7,-1}$	C2-H	-2.00	-1.23	-0.79	2.02
	C8-H	63.71	-24.98	-2.66	27.64
	O6-H	-1.17	-1.83	-1.49	3.32
	N7-H	11.75	-10.39	-6.23	16.61
	N9-H	-3.14	-8.35	-4.73	13.08
	N1	-0.06	-0.80	-0.74	1.55
	N3	1.44	-1.98	-1.75	3.73
	N7	2.36	-9.10	-8.74	17.83
	N9	0.80	-6.66	-6.20	12.85
Hx^0_{+6}	C2-H	2.12	-2.53	-0.19	2.72
	C8-H	-7.29	-4.43	-0.28	4.71
	O6-H	-8.13	-10.93	-6.96	17.89
	N1-H	1.03	-6.23	-5.25	11.48
	N9-H	1.74	-1.51	-0.12	1.63
	N1	-2.56	-4.90	-4.61	9.50
	N3	3.63	-4.96	-4.70	9.65
	N7	0.11	-1.14	-0.78	1.92
	N9	-2.16	-1.30	0.49	0.81
Experiment	C8-H	-18.1	-7.3	-1.9	9.3
	N1-H	-12.2	-9.1	-1.8	10.9
	N1	9.94	-6.10	-6.10	12.21
	N3	3.95	-3.25	-3.25	10.42
	N7	3.56	-5.29	-5.29	10.58

TABLE 10: Comparison of Experimental and Computed Eigenvectors for the O6-protonated Hx Structures Indicated

			as calculated			measured			
			$\langle a^*\rangle$	$\langle b\rangle$	$\langle c\rangle$	$\langle a^*\rangle$	$\langle b\rangle$	$\langle c\rangle$	$\delta\phi$ (deg)
			$Hx^{+1}_{+7,+6}$						
HN1	$\hat{V}_-$		−0.5236	−0.5204	0.6745	0.365	0.719	−0.591	15.44
	$\hat{V}_0$		0.8087	−0.0545	0.5857	0.858	−0.013	0.514	5.36
	$\hat{V}_+$		−0.2680	0.8522	0.4494	0.362	−0.695	−0.622	14.34
HC8	$\hat{V}_-$		−0.6390	−0.2418	0.7303	0.616	0.347	−0.707	6.36
	$\hat{V}_0$		0.7479	0.0266	0.6632	0.763	−0.038	0.646	3.57
	$\hat{V}_+$		−0.1798	0.9700	0.1639	0.197	−0.937	−0.288	7.47
			$Hx^0_{+6,+7,-9}$						
HN1	$\hat{V}_-$		−0.5624	−0.4803	0.6731	0.365	0.719	−0.591	18.48
	$\hat{V}_0$		0.8051	−0.1324	0.5782	0.858	−0.013	0.514	8.23
	$\hat{V}_+$		−0.1886	0.8671	0.4611	0.362	−0.695	−0.622	16.72
HC8	$\hat{V}_-$		−0.6700	−0.2020	0.7143	0.616	0.347	−0.707	8.95
	$\hat{V}_0$		0.7276	0.0122	0.6859	0.763	−0.038	0.646	3.81
	$\hat{V}_+$		−0.1473	0.9793	0.1388	0.197	−0.937	−0.288	9.39

Figure 5d, the contributions from radicals R1, R2, and R3 were 52.3%, 36.5%, and 11.3% respectively. Optimized fits at other orientations ($\langle a\rangle$ and $\langle c\rangle$) gave values sufficiently different that these should be considered only as estimates of the concentrations. We note that radicals R1 and R3 were suggested to be reduction products whereas R2 is the product of oxidation. Thus the estimated concentrations suggest an unexplained loss of oxidation products unless R3 somehow is a product of oxidation.

g-Tensors. A useful application of magnetic coupling parameters measured from radicals is the simulation of spectra from randomly oriented distributions for the purpose of analyzing spectra from powder or glass samples. To do so effectively,

EPR/ENDOR of Radical Formation in Purines

J. Phys. Chem. A, Vol. 109, No. 39, 2005 **8743**

TABLE 11: Gaussian Calculations for g Tensors for R1, R2, and R3 Formed in Hx·HCl·H$_2$O X-Irradiated at 10 K

			eigenvectors		
radical[a]	isotropic value	principal value	$\langle a* \rangle$	$\langle b \rangle$	$\langle c \rangle$
R1a	2.0028	2.0035	0.18842	0.96326	−0.19137
		2.0030	0.59390	−0.26695	−0.75896
		2.0018	0.78217	−0.02935	0.62238
R1b	2.0028	2.0034	0.15715	0.94695	−0.28035
		2.0031	0.65298	−0.31259	−0.68986
		2.0019	0.74089	0.07465	0.66746
R2	2.0045	2.0074	0.69846	−0.03767	−0.71465
		2.0039	0.01317	0.99912	−0.03979
		2.0022	0.71552	0.01838	0.69835
R3	2.0028	2.0039	0.36524	−0.86144	−0.35288
		2.0031	0.59435	0.50754	−0.62381
		2.0015	0.71648	0.01810	0.69737
		Directions from Crystal Structure			
base perpendicular			−0.71787	−0.02809	−0.69561

[a] R1a = Hx$^{+1}_{+7,+3}$, R1b = Hx$^{0}_{+3}$, R2 = Hx^{+1}, R3 = Hx$^{+1}_{+7,+6}$. See the text for discussion.
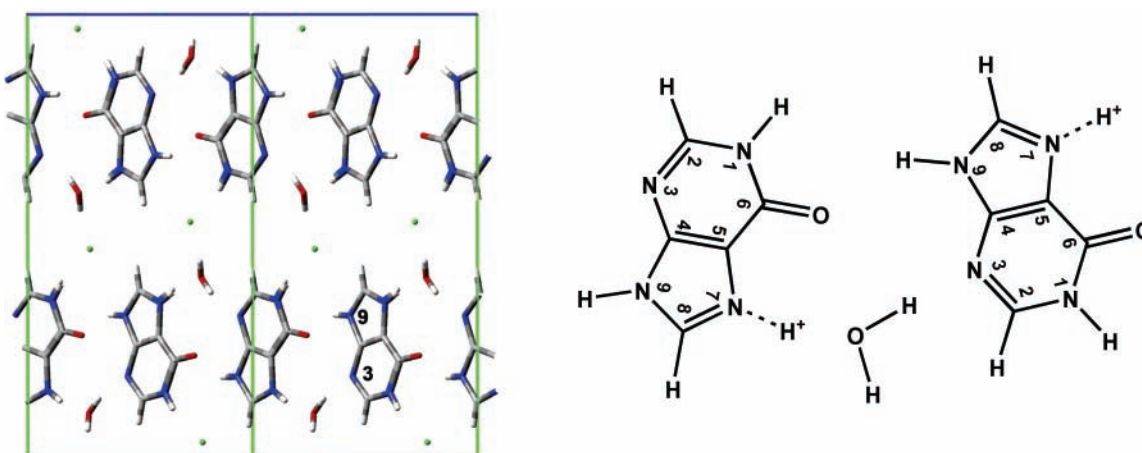
Figure 6. Illustration of molecular packing in Hx·HCl·H$_2$O crystals. Left: view along $\langle a \rangle$. $\langle b \rangle$ is vertical and $\langle c* \rangle$ is horizontal. The lower right structure has labels indicating atoms N3 and N9. Right: detail showing the packing motif consisting of a water molecule bridging HN9 to N3 of adjacent Hx$^{+1}_{+7}$ molecules. (In a full facial view, a layer either below or above the one illustrated is positioned with C8 directly below or above the oxygen of the water. See ref 6 for a discussion of this.)

it is necessary to know the **g**-tensor. However, **g**-tensors for carbon- and nitrogen-centered radicals have very little *g* anisotropy; as a result, it is difficult to make sufficiently accurate measurements to determine **g**-tensors experimentally. However, the Gaussian 03 suite includes **g**-tensor calculations (see Methods). The spectral features of R1 and R2, shown above in Figure 1a, are well separated and provide a means for testing the accuracy of the **g**-tensor calculations.

Table 11 shows the **g**-tensors calculated for the radical structures assigned for R1 and R2. (See the Methods section above for a description of the **g**-tensor calculation.) The calculations in fact predicted g_{eff} of 2.0074 for R2 at the crystal orientation used for Figure 1a whereas the value measured from the EPR and the simulation procedure was 2.0061. For R1 at the orientation for Figure 1a, the effective *g* was predicted to be 2.0030 and the value measured from the EPR and simulation procedures was 2.0027.

Proton-Transfer Processes. Although the primary focus of this report is on identification and description of the radical products, an element of the discussion in all cases was the molecular packing in the crystal and its role in their formation/stabilization. For example, R1 was identified as the product of net hydrogen addition to N3, possibility accompanied by deprotonation at N7; R2 as the product of deprotonation at N7; and, R3 as the product of net hydrogen addition to O6, probably

accompanied by deprotonation at N9. Figure 6 illustrates the molecular packing in the Hx·HCl·H$_2$O crystals as revealed by the X-ray diffraction study.[9] From the figure, the hydrogen bonding association between O6 of one molecule and HN9 of a neighbor are apparent. Equally apparent is the water-linked hydrogen bonding association between HN7 of one and N3 of another. Thus, the hydrogen bonding system in the crystal provides for the origin and destination of protons for the transfers indicated as the mechanisms by which the radicals were formed. A more complete and quantitative description of proton-transfer processes in this system will appear elsewhere.

Summary and Conclusions

In summary, therefore, low-temperature irradiation of Hx·HCl·H$_2$O crystals in four different degrees of deuteration led to three distinct radical species: R1, the product of net hydrogen addition to N3; R2, the product of net hydrogen loss from N7; and R3, the product of net hydrogen addition to O6. R1 exhibited magnetic parameters indicating nonplanarity of the bonding system to C2, a property also predicted by DFT-based calculations. The experimental results also indicated H/D isotope effects in the formation of all radicals, a property consistent with the proton-transfer mechanisms proposed as the processes by which the radicals were formed and stabilized in the crystals.

Supporting Information Available: Figure showing EPR and ENDOR results, angular dependence plots of the data, and additional tables showing computational results for R1 and R3. This material is available free of charge via the Internet at http://pubs.acs.org.

References and Notes

(1) Close, D. M. *Radiat. Res.* **1993**, *135*, 1.

(2) Cai, Z.; Gu, Z.; Sevilla, M. D. *J. Phys. Chem. B* **2000**, *104*, 10406.

(3) (a) Close, D. M.; Nelson, W. H. *Radiat. Res.* **1989**, *117*, 367. (b) Close, D. M.; Nelson, W. H.; Sagstuen, E.; Hole, E. O. *Radiat. Res.* **1994**, *137*, 300. (c) Nelson, W. H.; Sagstuen, E.; Hole, E. O.; Close, D. M. *Radiat. Res.* **1992**, *131*, 272.

(4) (a) Close, D. M.; Sagstuen, E.; Nelson, W. H. *J. Chem. Phys.* **1985**, *82*, 4386. (b) Close, D. M.; Nelson, W. H.; Sagstuen, E. *Radiat. Res.* **1987**, *112*, 283. (c) Close, D. M.; Sagstuen, E.; Nelson, W. H. *Radiat. Res.* **1988**, *116*, 379. (d) Sagstuen, E.; Hole, E. O.; Nelson, W. H.; Close, D. M. *Radiat. Res.* **1988**, *116*, 196. (e) Hole, E. O.; Sagstuen, E.; Nelson, W. H.; Close, D. M. *Radiat. Res.* **1991**, *125*, 119.

(5) Zehner, H.; Westhof, E.; Flossmann, W.; Müller, A. *Int. J. Radiat. Biol.* **1978**, *33*, 121.

(6) Tokdemir, S.; Nelson, W. H. *Radiat. Res.* **2005**, *163*, 663.

(7) Wong, J. L.; Keck, J. H., Jr. *J. Chem. Soc., Chem. Commun.* **1975**, 125.

(8) Lichtenberg, D.; Bergmann, F. *J. Chem. Soc., Perkin Trans. 1* **1973**, 789.

(9) Sletten, J.; Jensen, L. H. *Acta Crystallogr.* **1969**, *B25*, 1608.

(10) (a) Nelson, W. H.; Hole, E. O.; Sagstuen, E.; Close, D. M. *Int. J. Radiat. Biol.* **1988**, *54*, 963. (b) Kang, J.; Tokdemir, S.; Shao, J.; Nelson, W. H. *J. Magn. Reson.* **2003**, *165*, 128.

(11) Schonland, D. S. *Proc. Phys. Soc.* **1959**, *73*, 788.

(12) Duling, D. R. *J. Magn. Reson.* **1994**, *B104*, 105.

(13) Frisch, M. J.; Trucks, G. W.; Schlegel, H. B.; Scuseria, G. E.; Robb, M. A.; Cheeseman, J. R.; Montgomery, J. A., Jr.; Vreven, T.; Kudin, K. N.; Burant, J. C.; Millam, J. M.; Iyengar, S. S.; Tomasi, J.; Barone, V.; Mennucci, B.; Cossi, M.; Scalmani, G.; Rega, N.; Petersson, G. A.; Nakatsuji, H.; Hada, M.; Ehara, M.; Toyota, K.; Fukuda, R.; Hasegawa, J.; Ishida, M.; Nakajima, T.; Honda, Y.; Kitao, O.; Nakai, H.; Klene, M.; Li, X.; Knox, J. E.; Hratchian, H. P.; Cross, J. B.; Adamo, C.; Jaramillo, J.; Gomperts, R.; Stratmann, R. E.; Yazyev, O.; Austin, A. J.; Cammi, R.; Pomelli, C.; Ochterski, J. W.; Ayala, P. Y.; Morokuma, K.; Voth, G. A.; Salvador, P.; Dannenberg, J. J.; Zakrzewski, V. G.; Dapprich, S.; Daniels, A. D.; Strain, M. C.; Farkas, O.; Malick, D. K.; Rabuck, A. D.; Raghavachari, K.; Foresman, J. B.; Ortiz, J. V.; Cui, Q.; Baboul, A. G.; Clifford, S.; Cioslowski, J.; Stefanov, B. B.; Liu, G.; Liashenko, A.; Piskorz, P.; Komaromi, I.; Martin, R. L.; Fox, D. J.; Keith, T.; Al-Laham, M. A.; Peng, C. Y.; Nanayakkara, A.; Challacombe, M.; Gill, P. M. W.; Johnson, B.; Chen, W.; Wong, M. W.; Gonzalez, C.; Pople, J. A. *Gaussian 03*, revision B.04; Gaussian Inc.: Pittsburgh, PA, 2003.

(14) Vanhaelewyn, G. C. A. M.; Jansen, B.; Pauwels, E.; Sagstuen, E.; Waroquier, M.; Callens, F. J. *J. Phys. Chem. A* **2004**, *108*, 3308.

(15) (a) Törring, J. T.; Un, S.; Knupling, M.; Plato, M.; Möbius, K. *J. Chem. Phys.* **1997**, *107*, 3905. (b) Jayatilaka, D. *J. Chem. Phys.* **1998**, *108*, 7587.

(16) Bloembergen, N.; Shapiro, S.; Pershan, P. S.; Artman, J. O. *Phys. Rev.* **1959**, *114*, 445.

(17) McConnell, H. M.; Chesnut, D. B. *J. Chem. Phys.* **1958**, *28*, 107.

(18) Fessenden, R. W.; Schuler, R. H. *J. Chem. Phys.* **1963**, *39*, 2147.

(19) (a) Gordy, W. *Theory and Applications of Electron Spin Resonance*; Wiley: New York, 1980. (b) Bernhard, W. A. *J. Chem. Phys.* **1984**, *81*, 5928.

(20) Erling, P. A.; Nelson, W. H. *J. Phys. Chem. A* **2004**, *108*, 7591.

(21) Nelson, W. H.; Sagstuen, E.; Hole, E. O.; Close, D. M. *Radiat. Res.* **1998**, *149*, 75.

(22) The structural notation identifies the net charge (superscript) and the protonation state (subscript) relative to the neutral hypoxanthine structure. For example, $Hx^0_{+3,+7-9}$ indicates a charge of zero with protons added to N3 and N7, and with loss of the proton normally at N9.

(23) (a) Westheimer, F. H. *Chem. Rev.* **1961**, *61*, 265. (b) Kiefer, P. M.; Hynes, J. T. *J. Phys. Chem. A* **2003**, *107*, 9022.